Machine learning-assisted study on the thermal transport properties of two-dimensional M$_3$(C$_6$O$_6$)$_2$ (M = Fe, Co, Ni) materials

Meng-Jiao Teng[1] , **Li-Qin Deng**[2], **Pin-Zhen Jia**[2,*] **and Wu-Xing Zhou**[1,*]

[1] School of Materials Science and Engineering & Hunan Provincial Key Laboratory of Advanced Materials for New Energy Storage and Conversion, Hunan University of Science and Technology, Xiangtan 411201, People's Republic of China
[2] School of Science, Hunan Institute of Technology, Hengyang 421002, People's Republic of China

E-mail: pinzhenjia@hnu.edu.cn and wuxingzhou@hnu.edu.cn

CrossMark

Abstract

Two-dimensional metal-organic frameworks (MOF) are widely used in electronic devices and energy storage due to their large surface area, abundant active sites, and tunable sizes. A deeper understanding of the thermal transport properties of two-dimensional MOF materials is essential for these applications. In this work, we systematically studied the thermal transport properties of M$_3$(C$_6$O$_6$)$_2$ (M = Fe, Co, Ni) by using a machine learning interatomic potential method combined with the phonon Boltzmann transport equation. The results show that the lattice thermal conductivities of Fe$_3$(C$_6$O$_6$)$_2$, Co$_3$(C$_6$O$_6$)$_2$, and Ni$_3$(C$_6$O$_6$)$_2$ at room temperature are 4.0 W mK^{-1}, 5.5 W mK^{-1}, and 5.8 W mK^{-1}, respectively. The differences in thermal conductivity primarily arise from variations in phonon relaxation times, which can be elucidated by examining the three-phonon scattering phase space. Further analysis of bond strengths reveals that the strong bonding between Fe and O impedes phonon propagation through the oxygen atoms, resulting in lower lattice thermal conductivity. Our work provides a fundamental reference for understanding thermal transport in two-dimensional MOF.

Keywords: metal-organic frameworks (MOF), Boltzmann transport equation, thermal transport, machine learning potential

1. Introduction

In the technological revolution of the 21st century, nanomaterials are leading the field of materials science into a new era with their unique physical, chemical, and mechanical properties. In these materials, metal-organic frameworks (MOF) are widely used in aspects such as catalysis [1–3], biosensing [4–7], energy storage [8–11] and electronic devices [12] due to their high porosity, large specific surface area, structural diversity and tunable properties [13]. The MOF are crystalline materials formed by the self-assembly of metal ions or clusters coordinated by organic ligands through coordination bonds [14]. In recent decades, a large number of MOF material structures have been reported [15–21], which has promoted the development of MOF. With deepening research, scientists are increasingly focusing on 2D MOFs, which offer several advantages over their three-dimensional (3D) counterparts [22], including superior accessibility to metal active sites, larger specific surface areas and shorter

* Authors to whom any correspondence should be addressed.

ion transport distances [23]. However, the synthesis of high-quality large-area 2D MOF remains a significant challenge for their practical implementation. To address this challenge, Park *et al* [24] successfully synthesized a novel conductive 2D MOF known as copper hexahydroxybenzene ($Cu_3(C_6O_6)_2$) using a kinetically controlled approach with a competing coordination reagent. Additionally, Feng *et al* [11] reported a high-performance electrode based on a 2D MOF derived from hexaaminobenzene (HAB) represented by the formula $M_3(C_6N_6H_6)_2$ (M = Cu, Ni). Park *et al* [25] synthesized $Co_3(C_6N_6H_6)_2$, a novel cobalt-based two-dimensional conductive MOF that can be used as an electrode material for high-power energy storage devices. The advancements in the synthesis of $M_3(C_6X_6)_2$ (X = NH, O) represent a substantial step toward the practical application of MOF nanosheets.

The $M_3(C_6X_6)_2$ (X = NH, S, O) family have attracted much attention for their excellent performance in the fields of energy storage and electrocatalysis mainly due to their presence of active open metal sites and abundant redox active centers [24]. Feng *et al* [11] investigated a submillimeter-thick $Ni_3(C_6N_6H_6)_2$ MOF electrode that demonstrated a high volumetric capacitance of up to 760 F cm^{-3} and an areal capacitance exceeding 20 F cm^{-2}. It also exhibited highly reversible redox behavior, maintaining a capacitance retention of 90% after 12 000 cycles. Gao *et al* [26] reported a 2D MOF $Cu_3(C_6O_6)_2$-iodine cathode for high-performance NH_4^+ hybrid supercapacitors (HSCs). The $Cu_3(C_6O_6)_2/I_2$ electrode achieved an areal capacitance of 111.7 mF cm^{-2} at a current density of 0.4 mA cm^{-2}. Combined with a porous P-MXene anode, the HSCs achieved an outstanding areal energy density of 31.5 mWh cm^{-2} at 400 mW cm^{-2} and maintained 89.5% capacity after 10 000 cycles. Wang *et al* [27] reported a surfactant-assisted solution synthesis of ultrathin 2D conjugated MOF nanosheets $Cu_3(C_6O_6)_2$. As a cathode material in lithium-ion batteries, $Cu_3(C_6O_6)_2$ nanosheets exhibited enhanced surface area and shortened ion/electron diffusion paths. Consequently, $Cu_3(C_6O_6)_2$ nanosheets exhibit high lithium-ion storage performance with a specific capacity of 153 mAh g^{-1}, charging to 81% within 3 min at 1.0 A/g, and retaining 90% capacity after 10 000 cycles. Despite the significant advancements in research endeavors focusing on $M_3(C_6X_6)_2$ materials within these domains, our understanding of their thermal conductivity remains relatively limited. The thermal transport properties of materials are critical for their performance in thermoelectric devices and thermal energy conversion applications [28, 29]. Traditional 3D MOF often feature complex porous structures and larger volumes that impede effective thermal transport [22]. In contrast, 2D MOFs with atomic-layer thickness offer shorter heat transfer pathways and improve efficiency [23]. Moreover, the thermal conductivity of 2D MOF can be finely tuned by modifying metal nodes, organic ligands, or interlayer interactions, providing opportunities for designing materials with specific thermal transport characteristics.

This study systematically investigates the thermal transport properties of $M_3(C_6O_6)_2$ (M = Fe, Co, Ni) by using a machine learning interatomic potential (MLIP) method combined with the phonon Boltzmann transport equation (PBTE). At a temperature of 300 K, the lattice thermal conductivities of $Fe_3(C_6O_6)_2$, $Co_3(C_6O_6)_2$ and $Ni_3(C_6O_6)_2$ are 4.0 W mK^{-1}, 5.4 W mK^{-1}, and 5.8 W mK^{-1}, respectively. Through analysis, the differences in thermal conductivity are mainly attributed to varying phonon relaxation times. $Fe_3(C_6O_6)_2$ exhibits a large three-phonon scattering phase space, indicating the presence of numerous scattering channels, which result in shorter relaxation times. Further analysis of the crystal orbital Hamiltonian population (pCOHP) indicates that the strong Fe-O bonds in $Fe_3(C_6O_6)_2$ significantly impede phonon propagation through oxygen atoms, leading to lower thermal conductivity. Our research findings provide insights into the phonon thermal transport properties of MOF.

2. Computation method

Density functional theory (DFT)-based first-principles calculations were performed utilizing the Vienna *ab initio* simulation package [30–33], which relies on pseudo-potentials and plane wave basis functions. The exchange-correlation functional utilized was the generalized gradient approximation in the Perdew–Burke–Ernzerhof formulation [34]. During structural optimization, all crystal structures were fully relaxed using a $3 \times 3 \times 1$ k-point grid with the total energy and force convergence criteria set to 10^{-6} eV and 10^{-2} eV $Å^{-1}$, respectively, and a plane wave kinetic energy cutoff of 550 eV. Additionally, the spin polarization of Fe, Co, and Ni was considered in all calculations. To mitigate interactions between layers, a vacuum layer of 20 Å was introduced. Moment tensor potential (MTP) can predict the energy, forces, and stresses of the material system with an accuracy comparable to that of quantum mechanical *ab initio* methods [35–38]. Consequently, the resulting force field parameters can effectively predict the thermal transport properties of the material [39, 40]. In order to obtain MTP [39], an *ab initio* computational molecular dynamics (AIMD) simulation with a time step of 1 fs and a duration of 1 ps was conducted using a $2 \times 2 \times 1$ supercell of $M_3(C_6O_6)_2$ at a temperature of 300 K. Furthermore, 400 configurations were extracted from the motion trajectory as the training dataset for MLIP packets and the fitting weights for energy, force, and stress were set to 1, 0.1, and 0.001 respectively, with the maximum number of iterations configured at 3000 to ensure convergence of the MTP training within 3000 steps [41]. As demonstrated in previous research [42, 43], the MTP can be utilized to reduce the significant computational expense involved in calculating second-order force constants (2nd-FC) and third-order force constants (3rd-FC) through DFT [44, 45]. The accuracy of MTP in calculating the thermal transport properties of materials has been shown to closely match that of the DFT method [40, 44]. Furthermore, 2nd-FC and phonon dispersion were calculated using MTP in conjunction with the Phonopy software package [46], while 3rd-FC were derived from MTP and $3 \times 3 \times 1$ supercells [42]. Combined with 2nd-FC and 3rd-FC, the lattice thermal conductivity was iteratively solved using

the PBTE with the ShengBTE software package, employing an $18 \times 18 \times 1$ k-grid to ensure the convergence of thermal conductivity [47, 48].

3. Results and discussion

$M_3(C_6O_6)_2$ (M = Fe, Co, Ni) exhibits a two-dimensional planar network structure, with each basic unit comprising two benzene rings and three MO_4 units. As shown in figures 1(a) and (b), the lattice vectors of the primitive unit cell of $M_3(C_6O_6)_2$ satisfy the conditions of $a = b$ and $\alpha = \beta = 90°$, with $\gamma = 60°$. The optimized lattice parameters for $Fe_3(C_6O_6)_2$, $Co_3(C_6O_6)_2$, and $Ni_3(C_6O_6)_2$ are $a = b = 13.161$ Å, $a = b = 13.041$ Å, and $a = b = 12.994$ Å, respectively. These values are consistent with previous reported [49]. To investigate the stability of the material at high temperature, 1 ps of AIMD simulations were performed with a time step of 1 fs at 800 K. The total energy curves of the three materials over time are presented in figure 1(c). It is evident that the three materials exhibit a stabilizing trend around 100 fs with their energy curves subsequently approaching a straight line, indicating the high-temperature tolerance of the $M_3(C_6O_6)_2$ (M = Fe, Co, Ni) structures. Additionally, the phonon dispersion relations of $M_3(C_6O_6)_2$ (M = Fe, Co, Ni) were calculated by MTP, as shown in figure 2. The lack of imaginary frequencies within the phonon spectrum confirms dynamic stability of the $M_3(C_6O_6)_2$ (M = Fe, Co, Ni) structures. The phonon frequencies of the three materials fall within the range of 0–43 THz, and a noticeable band gap appears in the phonon spectra due to the significant differences in the masses of the constituent elements. To verify the accuracy of the MTP we obtained, we used the $M_3(C_6O_6)_2$ structural component validation set and calculated the energy and atomic forces of the $M_3(C_6O_6)_2$ structure using both MTP and DFT methods. Form figure 3(a) to figure 3(f), we can find that the accuracy of the MTP we obtained is highly consistent with the DFT structure. Based on the theoretical foundation of our research, we have demonstrated the dynamic and thermodynamic stability of the $M_3(C_6O_6)_2$ structure through phonon dispersion relations and AIMD. In addition, the $M_3(C_6O_6)_2$ structure has been successfully synthesized experimentally by Park *et al* [24], indicating that the $M_3(C_6O_6)_2$ structure can indeed exist stably in nature, which to some extent demonstrates the rationality of our theoretical research.

$M_3(C_6O_6)_2$ has been successfully synthesized and has demonstrated significant application potential in various fields. In these applications, thermal conductivity has become a non-negligible material property. Therefore, a systematic study of the thermal transport properties of $M_3(C_6O_6)_2$ is of great importance for its application and material design. For this purpose, we systematically studied the thermal transport properties of $M_3(C_6O_6)_2$ based on the PBTE. Firstly, we provide the lattice thermal conductivity of $M_3(C_6O_6)_2$ along different crystallographic orientations at room temperature, as shown in table 1. The lattice thermal conductivities of

$M_3(C_6O_6)_2$ (M = Fe, Co, Ni) along the *xx*- (*a* direction) and *yy*- (vertical *a* direction) directions were calculated at room temperature. Due to the hexagonal honeycomb framework of the $M_3(C_6O_6)_2$ crystal structure, the *xx*- orientation can be regarded as the zigzag direction of the hexagonal lattice, while the *yy*- orientation corresponds to the armchair direction. The significant differences in atomic arrangements along these orientations lead to difference in the ability of phonons to propagate along different directions, resulting in the anisotropic lattice thermal conductivity of the $M_3(C_6O_6)_2$ structure. Therefore, the results of these materials exhibits anisotropy, with the highest value observed along the *xx*- direction. In figure 4(a), the thermal conductivity of $M_3(C_6O_6)_2$ (M = Fe, Co, Ni) was calculated over a temperature range of 100 K to 800 K. The lattice thermal conductivity of the three materials decreases with increasing temperature, following the relationship $\kappa_p(Fe_3(C_6O_6)_2) < \kappa_p(Co_3(C_6O_6)_2) < \kappa_p(Ni_3(C_6O_6)_2)$. To elucidate the differences in thermal conductivity, we calculated the frequency-dependent cumulative thermal conductivity in figure 4(b). The results indicate that the primary contribution to lattice thermal conductivity arises from low-frequency phonons (0–10 THz). Therefore, our subsequent analysis will concentrate on the thermal transport properties of phonon with frequencies below 10 THz. Additionally, we have provided the cumulative lattice thermal conductivity as a function of the mean free path, as shown in figure 4(c). We found that the mean free path of heat-carrying phonons in the $M_3(C_6O_6)_2$ structure range from 0.01 to 0.1 μm. Interestingly, phonon modes with mean free paths between 0.01 and 0.1 μm contribute more to the total thermal conductivity in $Co_3(C_6O_6)_2$ than in $Ni_3(C_6O_6)_2$. However, $Ni_3(C_6O_6)_2$ exhibits some phonon modes with exceptionally long mean free path (>1 μm), which contribute an additional ~18% to the lattice thermal conductivity, resulting in a higher overall lattice thermal conductivity for $Ni_3(C_6O_6)_2$ compared to $Co_3(C_6O_6)_2$. From the perspective of PBTE, firstly, we calculated the group velocity of $M_3(C_6O_6)_2$ (M = Fe, Co, Ni) at 300 K. As shown in figures 5(a)–(c), the group velocity differences among the three materials are negligible, indicating that group velocity has little effect on the variations in lattice thermal conductivity.

In addition, according to the qualitative empirical formula $\kappa \sim 1/3C_v v^2 \tau$, C_v, v and τ are the heat capacity group velocity, and relaxation time respectively. The C_v is a constant above a certain temperature, so the relaxation time is another critical parameter influencing thermal conductivity [50, 51]. Form figure 6(a), it is not difficult to observe that the relaxation time of phonons in $Co_3(C_6O_6)_2$ and $Ni_3(C_6O_6)_2$ is generally almost identical, but the relaxation time of phonons in $Fe_3(C_6O_6)_2$ is significantly lower than that of phonons in $Co_3(C_6O_6)_2$ and $Ni_3(C_6O_6)_2$. To explain this phenomenon, we provide the weighted scattering phase space for each phonon mode in figure 6(b) to quantitatively compare the number of processes allowed for phonon mode scattering in different structures at 300 K [52, 53]. As illustrated in figure 6(b), the three-phonon scattering
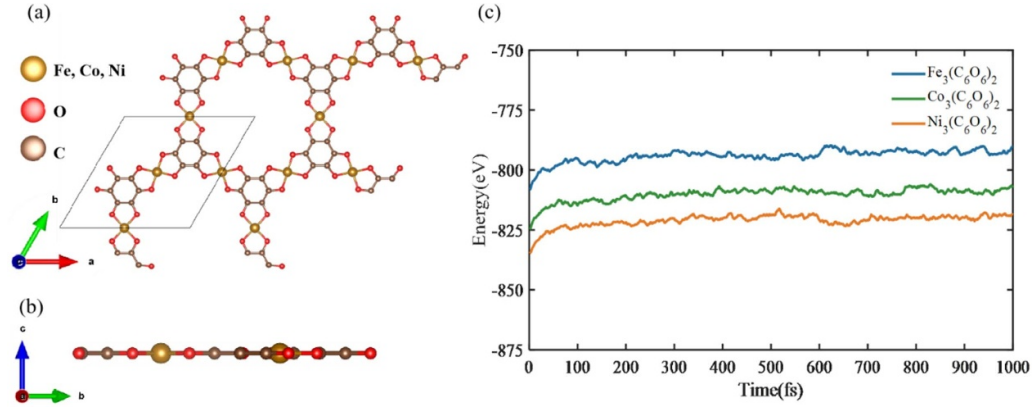
Figure 1. (a) Top view and (b) side view of the $M_3(C_6O_6)_2$ (M = Fe, Co, Ni) structures. (c) The total energy of $M_3(C_6O_6)_2$ versus time.
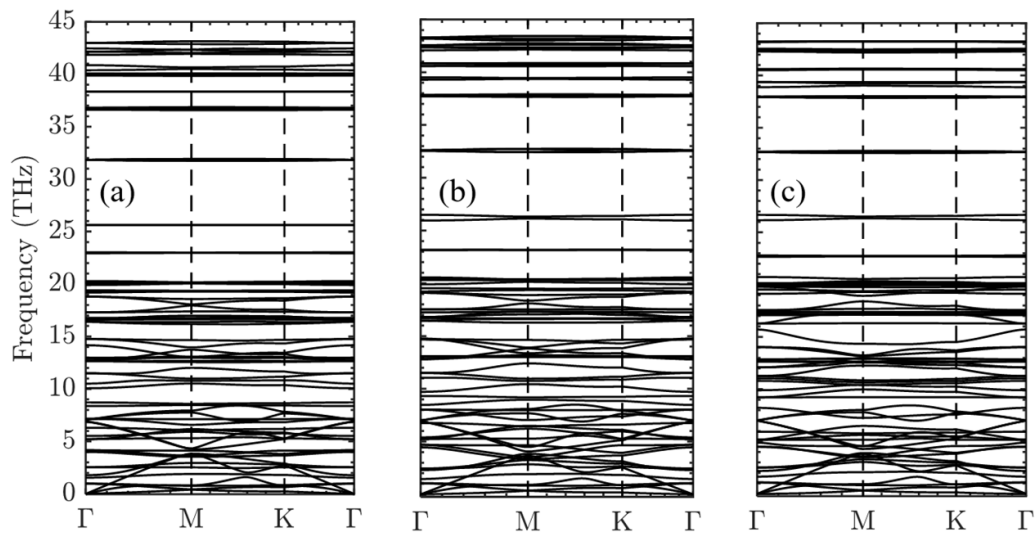

Figure 2. The phonon spectra of (a) $Fe_3(C_6O_6)_2$, (b) $Co_3(C_6O_6)_2$, and (c) $Ni_3(C_6O_6)_2$.
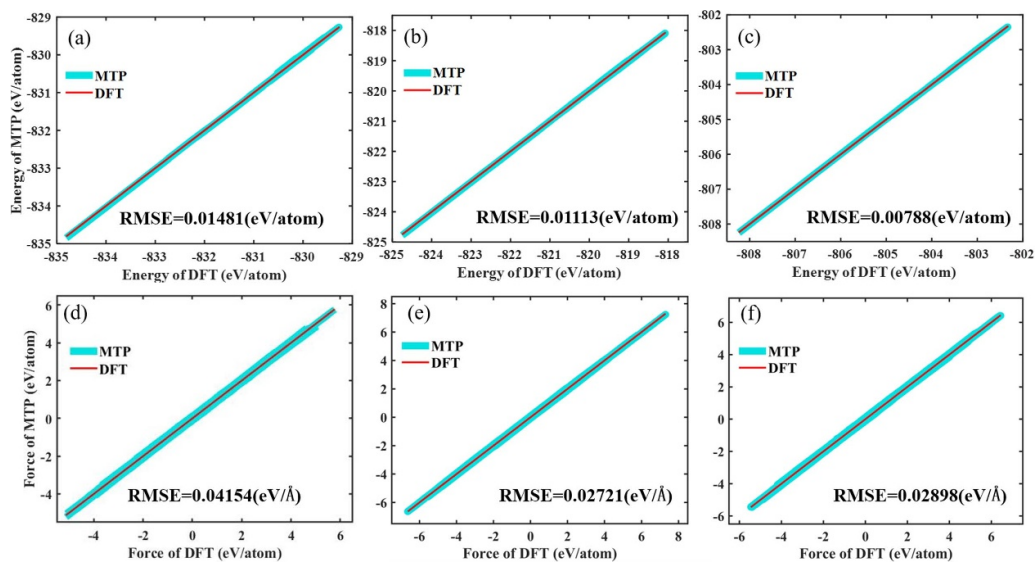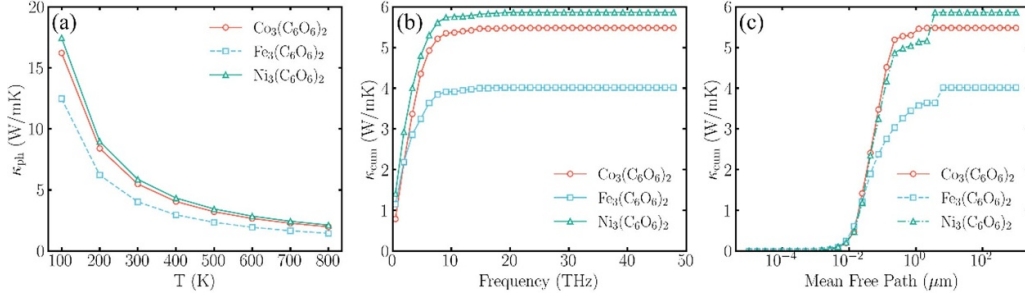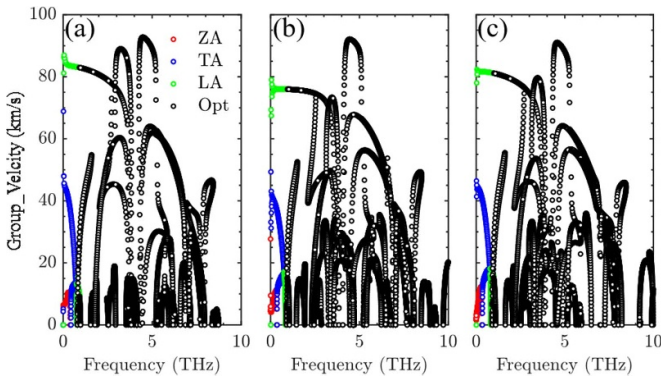

Figure 3. The energy of the (a) $Fe_3(C_6O_6)_2$, (b) $Co_3(C_6O_6)_2$, and (c) $Ni_3(C_6O_6)_2$ structure using both MTP and DFT methods; And the atomic forces of the (d) $Fe_3(C_6O_6)_2$, (e) $Co_3(C_6O_6)_2$, and (f) $Ni_3(C_6O_6)_2$ structure using both MTP and DFT methods.

Table 1. Lattice thermal conductivity of $M_3(C_6O_6)_2$ (M = Fe, Co, Ni) along the *xx-*, *yy*-directions at 300 K.

	Lattice thermal conductivity (W mK^{-1})	
	κ_{xx}	κ_{yy}
$Fe_3(C_6O_6)_2$	4.015	3.648
$Co_3(C_6O_6)_2$	5.481	4.887
$Ni_3(C_6O_6)_2$	5.864	5.552

Figure 4. (a) Lattice thermal conductivity of $M_3(C_6O_6)_2$ (M = Fe, Co, Ni); (b) Frequency dependence of the cumulative thermal conductivity of $M_3(C_6O_6)_2$ (M = Fe, Co, Ni); (c) Mean Free Path of the cumulative thermal conductivity of $M_3(C_6O_6)_2$ (M = Fe, Co, Ni).

Figure 5. Group velocities of (a) $Fe_3(C_6O_6)_2$, (b) $Co_3(C_6O_6)_2$, (c) $Ni_3(C_6O_6)_2$.

phase space for $Fe_3(C_6O_6)_2$ is significantly larger than that for $Co_3(C_6O_6)_2$ and $Ni_3(C_6O_6)_2$. However, the scattering channels of $Co_3(C_6O_6)_2$ and $Ni_3(C_6O_6)_2$ are generally similar, which is completely consistent with the relationship between relaxation time. This observation indicates that $Ni_3(C_6O_6)_2$ and $Co_3(C_6O_6)_2$ have relatively fewer phonon scattering channels, longer phonon relaxation times, and thus exhibit higher thermal conductivity. The slight difference in thermal conductivity between Ni and Co is due to the presence of a small number of long mean free path phonon modes in the Ni system (figure 4(c)).

In order to further investigate the reasons for the thermal conductivity differences between $M_3(C_6O_6)_2$, we studied the causes of thermal conductivity differences from the perspective of structural differences. The difference between $M(C_6O_6)_2$ is only reflected in the fact that the M–O bonds, formed by different metal atom, have different bond strength, and the bond strength between atoms have a significant impact on the propagation of phonons. In addition, it is not difficult to observe through the phonon density of states of $M(C_6O_6)_2$ that

the vast majority of vibration modes involve O atoms, followed by transition metal atoms. As shown in figures 7(a)–(c). This indicates that the bonding strength (BS) of M–O bonds formed by the combination of different metal atoms and O atoms is the main reason affecting phonon propagation. Therefore, the substitution of metal atoms in the MO_4 ligand alters the vibrational modes of O atoms to a certain extent. The greater the M–O BS, the stronger the interaction between them becomes. The greater the impact on the vibration modes of O atoms, which will consequently increase the difficulty of phonon propagation and reduce the thermal conductivity. To verify this, the Lobster package [54] was employed to calculate the projected crystal orbital Hamilton population (pCOHP) of Fe, Co, and Ni bonded with O in figure 8(a). The -pCOHP serves as a tool for identifying bonding types, with positive values indicating bond promotion and negative values indicating bond disruption [55]. The Ni–O bond exhibits an anti-bonding state in the energy range of -2.5–0 eV, while both the Fe–O and Co–O bonds manifest bonding states, suggesting that the Ni–O bond is comparatively weaker. However, the Fe–O bond displays higher peaks at approximately -3.75 eV and -8.15 eV, corresponding to a larger integral value of $-$pCOHP, which signifies stronger bonding. Notably, the bonding components across the three structures remain similar. Furthermore, the integral of $-$pCOHP (denoted as $-$ICOHP) was calculated to quantify the BS between Fe, Co, and Ni and O, as presented in figure 8(b). The -ICOHP values for the chemical bonds Fe–O, Co–O, and Ni–O are 2.78, 2.60, and 2.34, respectively. This BS relationship of BS(Fe-O) > BS(Co-O) > BS(Ni-O) is inversely correlated with the lattice thermal conductivity of the corresponding structures, which follows the order of $\kappa_p(Fe_3(C_6O_6)_2) < \kappa_p(Co_3(C_6O_6)_2) < \kappa_p(Ni_3(C_6O_6)_2)$. Consequently, the strong BS between Fe and O in these three materials significantly affects the vibration of oxygen atoms, thereby hindering the propagation of phonon and reducing the thermal conductivity.
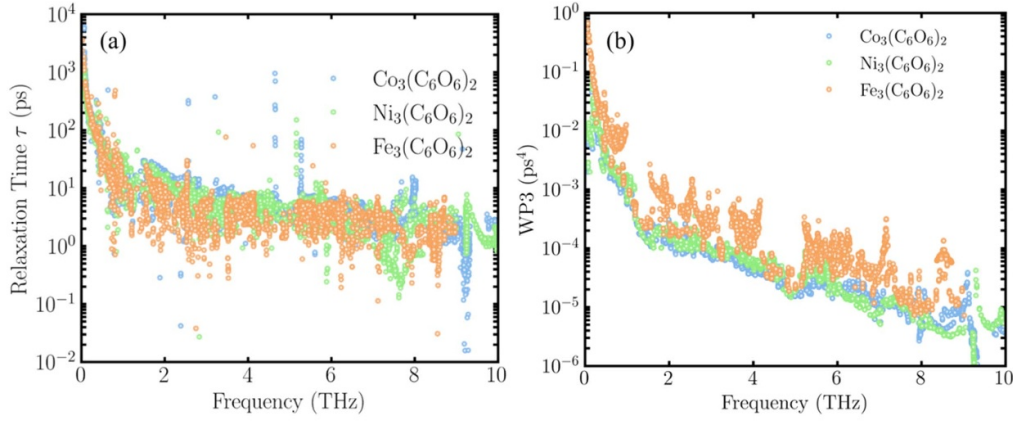
Figure 6. (a) Phonon relaxation time and (b) three-phonon scattering phase space of $M_3(C_6O_6)_2$ (M = Fe, Co, Ni) at 300 K.
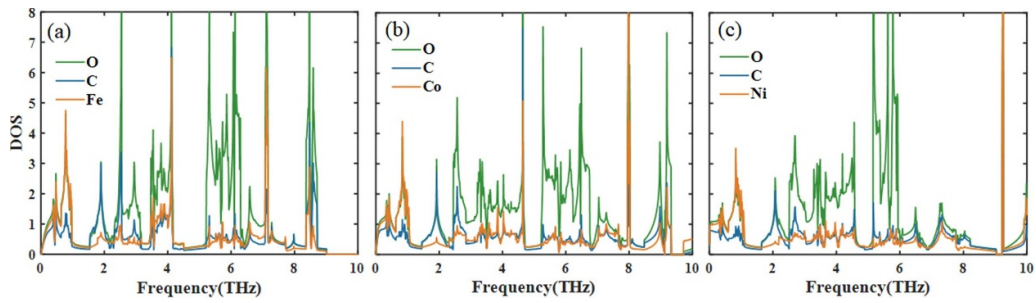

Figure 7. Phonon density of states of (a) $Fe_3(C_6O_6)_2$, (b) $Co_3(C_6O_6)_2$, (c) $Ni_3(C_6O_6)_2$.
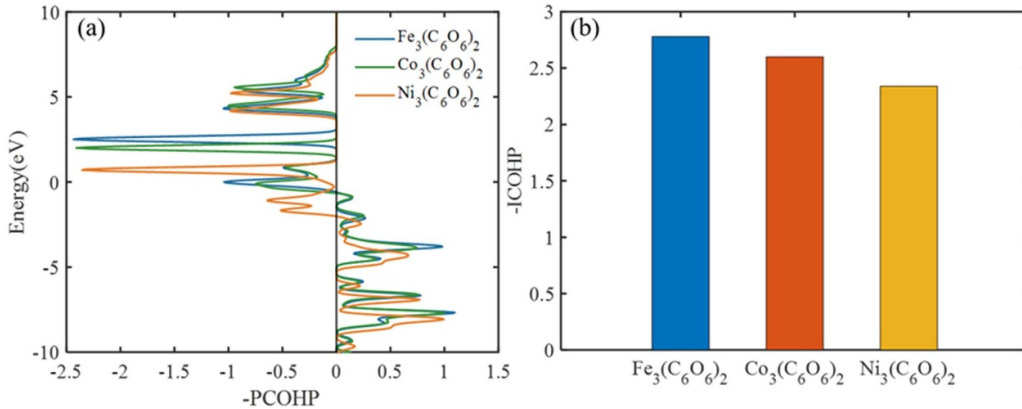

Figure 8. (a) $-$pCOHP and (b) $-$ICOHP of the M–O bonds.

4. Conclusions

In conclusion, we systematically investigated the thermal transport properties of $M_3(C_6O_6)_2$ (M = Fe, Co, Ni) by using a MLIP method combined with the PBTE. The thermal conductivities of $Fe_3(C_6O_6)_2$ and $Co_3(C_6O_6)_2$ exhibit 4.0 W mK^{-1} and 5.5 W mK^{-1} at room temperature, while the thermal conductivity of $Ni_3(C_6O_6)_2$ displays 5.8 W mK^{-1}. The analysis demonstrates that the differences in thermal conductivity among the three materials can be attributed to phonon relaxation times. A larger scattering phase space indicates more phonon scattering channels, leading to decreased relaxation

time and reduced thermal conductivity in $Fe_3(C_6O_6)_2$. The thermal transport of $M_3(C_6O_6)_2$ (M = Fe, Co, Ni) is mainly through the O atoms. Further analysis of pCOHP and the $-$ICOHP values demonstrate that the strong Fe–O bonds in $Fe_3(C_6O_6)_2$ hinder the propagation of phonon, resulting in a reduced thermal conductivity.

Data availability statement

The data that support the findings of this study are available upon reasonable request from the authors.

Acknowledgment

ORCID iDs

Meng-Jiao Teng https://orcid.org/0009-0005-1076-0147
Wu-Xing Zhou https://orcid.org/0000-0002-6006-8248

References

[1] Zuo X, Chang K, Zhao J, Xie Z, Tang H, Li B and Chang Z 2016 Bubble-template-assisted synthesis of hollow fullerene-like MoS $_2$ nanocages as a lithium ion battery anode material *J. Mater. Chem.* A **4** 51–58

[2] Ma X, Liu H, Yang W, Mao G, Zheng L and Jiang H-L 2021 Modulating coordination environment of single-atom catalysts and their proximity to photosensitive units for boosting MOF photocatalysis *J. Am. Chem. Soc.* **143** 12220–9

[3] Zhang C, Lei D, Xie C, Hang X, He C and Jiang H 2021 Piezo-photocatalysis over metal–organic frameworks: Promoting photocatalytic activity by piezoelectric effect *Adv. Mater.* **33** 2106308

[4] Shi M-Y, Xu M and Gu Z-Y 2019 Copper-based two-dimensional metal-organic framework nanosheets as horseradish peroxidase mimics for glucose fluorescence sensing *Anal. Chim. Acta* **1079** 164–70

[5] Ko M, Aykanat A, Smith M and Mirica K 2017 Drawing sensors with ball-milled blends of metal-organic frameworks and graphite *Sensors* **17** 2192

[6] Yao M, Lv X, Fu Z, Li W, Deng W, Wu G and Xu G 2017 Layer-by-layer assembled conductive metal–organic framework nanofilms for room-temperature chemiresistive sensing *Angew. Chem., Int. Ed.* **56** 16510–4

[7] Smith M K and Mirica K A 2017 Self-organized frameworks on textiles (SOFT): Conductive fabrics for simultaneous sensing, capture, and filtration of gases *J. Am. Chem. Soc.* **139** 16759–67

[8] Wang F, Cai J, Yang C, Luo H, Li X, Hou H, Zou G and Zhang D 2023 Improved capacitive energy storage nanocomposites at high temperature utilizing ultralow loading of bimetallic MOF *Small* **19** 2300510

[9] Liu N, Liu X and Pan J 2022 A new rapid synthesis of hexagonal prism Zn-MOF as a precursor at room temperature for energy storage through pre-ionization strategy *J. Colloid Interface Sci.* **606** 1364–73

[10] Qin Z, Xu Y, Liu L, Liu M, Zhou H, Xiao L, Cao Y and Chen C 2022 Ni-MOF composite polypyrrole applied to supercapacitor energy storage *RSC Adv.* **12** 29177–86

[11] Feng D *et al* 2018 Robust and conductive two-dimensional metal−organic frameworks with exceptionally high volumetric and areal capacitance *Nat. Energy* **3** 30–36

[12] Wu G, Huang J, Zang Y, He J and Xu G 2017 Porous field-effect transistors based on a semiconductive metal–organic framework *J. Am. Chem. Soc.* **139** 1360–3

[13] Zhou H-C J and Kitagawa S 2014 Metal–Organic Frameworks (MOFs) *Chem. Soc. Rev.* **43** 5415–8

[14] Liu W, Li Y, Wang Y and Feng Y 2024 Bioactive metal–organic frameworks as a distinctive platform to diagnosis and treat vascular diseases *Small* **20** 2310249

[15] Xiang Y, Cheng C-Y, Liu M-H, Bai W-C, Zang Z-X, Xu L, Yu Y and Liu G-J 2024 Efficient recovery of gold using Macroporous Metal-Organic framework prepared by the "MOF in MOF" method *Sep. Purif. Technol.* **335** 126131

[16] Liu X, Wang K, Chang Z, Zhang Y, Xu J, Zhao Y S and Bu X 2019 Engineering donor–acceptor heterostructure metal–organic framework crystals for photonic logic computation *Angew. Chem., Int. Ed.* **58** 13890–6

[17] Yu M-H *et al* 2019 Enhanced gas uptake in a microporous metal–organic framework via a sorbate induced-fit mechanism *J. Am. Chem. Soc.* **141** 17703–12

[18] Chen Q, Xian S, Dong X, Liu Y, Wang H, Olson D H, Williams L J, Han Y, Bu X and Li J 2021 High-efficiency separation of *n* -Hexane by a dynamic metal-organic framework with reduced energy consumption *Angew. Chem., Int. Ed.* **60** 10593–7

[19] Cui W, Hu T and Bu X 2020 Metal–organic framework materials for the separation and purification of light hydrocarbons *Adv. Mater.* **32** 1806445

[20] Pang J, Wu M, Qin J-S, Liu C, Lollar C T, Yuan D, Hong M and Zhou H-C 2019 Solvent-assisted, thermally triggered structural transformation in flexible mesoporous metal–organic frameworks *Chem. Mater.* **31** 8787–93

[21] Li B, Zhao Y-M, Kirchon A, Pang J-D, Yang X-Y, Zhuang G-L and Zhou H-C 2019 Unconventional method for fabricating valence tautomeric materials: integrating redox center within a metal–organic framework *J. Am. Chem. Soc.* **141** 6822–6

[22] Wang S, McGuirk C M, d'Aquino A, Mason J A and Mirkin C A 2018 Metal–organic framework nanoparticles *Adv. Mater.* **30** 1800202

[23] Xiong D, Deng X, Cao Z, Tao S, Song Z, Xiao X, Deng W, Hou H, Zou G and Ji X 2023 2D metal–organic frameworks for electrochemical energy storage *Energy Environ. Mater.* **6** e12521

[24] Park J, Hinckley A C, Huang Z, Feng D, Yakovenko A A, Lee M, Chen S, Zou X and Bao Z 2018 Synthetic routes for a 2D semiconductive copper hexahydroxybenzene metal–organic framework *J. Am. Chem. Soc.* **140** 14533–7

[25] Park J, Lee M, Feng D, Huang Z, Hinckley A C, Yakovenko A, Zou X, Cui Y and Bao Z 2018 Stabilization of hexaaminobenzene in a 2D conductive metal–organic framework for high power sodium storage *J. Am. Chem. Soc.* **140** 10315–23

[26] Gao M *et al* 2023 2D conjugated metal–organic frameworks embedded with iodine for high-performance ammonium-ion hybrid supercapacitors *Adv. Mater.* **35** 2305575

[27] Wang Z *et al* 2020 Ultrathin two-dimensional conjugated metal–organic framework single-crystalline nanosheets enabled by surfactant-assisted synthesis *Chem. Sci.* **11** 7665–71

[28] Chen X-K, Zhang Y, Luo Q-Q, Jia P-Z and Zhou W-X 2025 Strain-driven anisotropic enhancement in the thermal conductivity of KCaBi: the role of optical phonons *Int. J. Heat Mass Transfer* **236** 126364

[29] Xie Z, Chen X, Yu X, Zhang Y, Wang H and Zhang L 2017 Reduction of phonon thermal conduction in isotopic graphene nanoribbon superlattices *Sci. China Phys. Mech. Astron.* **60** 107821

[30] Kresse G and Furthmüller J 1996 Efficient iterative schemes for *ab initio* total-energy calculations using a plane-wave basis set *Phys. Rev.* B **54** 11169–86

[31] Kresse G and Joubert D 1999 From ultrasoft pseudopotentials to the projector augmented-wave method *Phys. Rev.* B **59** 1758–75

[32] Jia P-Z, Xie Z-X, Deng Y-X, Zhang Y, Tang L-M, Zhou W-X and Chen K-Q 2022 High thermoelectric performance induced by strong anharmonic effects in monolayer (PbX)2 (X = S, Se, Te) *Appl. Phys. Lett.* **121** 043901

[33] Jia P-Z, Zeng Y-J, Wu D, Pan H, Cao X-H, Zhou W-X, Xie Z-X, Zhang J-X and Chen K-Q 2020 Excellent thermoelectric performance induced by interface effect in MoS_2 /$MoSe_2$ van der Waals heterostructure *J. Phys.: Condens. Matter* **32** 055302

[34] Perdew J P, Burke K and Ernzerhof M 1996 Generalized gradient approximation made simple *Phys. Rev. Lett.* **77** 3865–8

[35] Mueller T, Hernandez A and Wang C 2020 Machine learning for interatomic potential models *J. Chem. Phys.* **152** 050902

[36] Deringer V L, Caro M A and Csányi G 2019 Machine learning interatomic potentials as emerging tools for materials science *Adv. Mater.* **31** 1902765

[37] Zhou W-X, Wu C-W, Cao H-R, Zeng Y-J, Xie G and Zhang G 2025 Abnormal thermal conductivity increase in β-Ga_2O_3 by an unconventional bonding mechanism using machine-learning potential *Mater. Today Phys.* **52** 101677

[38] Kuang H-L, Wu C-W, Zeng Y-J, Chen X-K and Zhou W-X 2024 The amplification effect of four-phonon scattering in CdX (X = Se, Te): the role of mid-frequency phonons *Int. J. Therm. Sci.* **205** 109254

[39] Mishin Y 2021 Machine-learning interatomic potentials for materials science *Acta Mater.* **214** 116980

[40] Novoselov I I, Yanilkin A V, Shapeev A V and Podryabinkin E V 2019 Moment tensor potentials as a promising tool to study diffusion processes *Comput. Mater. Sci.* **164** 46–56

[41] Novikov I S, Gubaev K, Podryabinkin E V and Shapeev A V 2021 The MLIP package: Moment tensor potentials with MPI and active learning *Mach. Learn.* **2** 025002

[42] Wu C-W, Ren X, Li S-Y, Zeng Y-J, Zhou W-X and Xie G 2022 Significant regulation of stress on the contribution of optical phonons to thermal conductivity in layered Li_2ZrCl_6: First-principles calculations combined with the machine-learning potential approach *Appl. Phys. Lett.* **121** 172201

[43] Chen A, Tong H, Wu C-W, Xie G, Xie Z-X, Xiang C-Q and Zhou W-X 2023 Stress effect on lattice thermal conductivity of anode material $NiNb_2O_6$ for lithium-ion batteries *Chin. Phys.* B **32** 058201

[44] Mortazavi B, Podryabinkin E V, Novikov I S, Rabczuk T, Zhuang X and Shapeev A V 2021 Accelerating first-principles estimation of thermal conductivity by machine-learning interatomic potentials: a MTP/ShengBTE solution *Comput. Phys. Commun.* **258** 107583

[45] Mortazavi B, Novikov I S, Podryabinkin E V, Roche S, Rabczuk T, Shapeev A V and Zhuang X 2020 Exploring phononic properties of two-dimensional materials using machine learning interatomic potentials *Appl. Mater. Today* **20** 100685

[46] Togo A and Tanaka I 2015 First principles phonon calculations in materials science *Scr. Mater.* **108** 1–5

[47] Li W *et al* 2014 ShengBTE: a solver of the Boltzmann transport equation for phonons *Comput. Phys. Commun.* **185** 1747–58

[48] Xie Z-X, Zhang Y, Zhang L-F and Fan D-Y 2017 Effect of topological line defects on electron-derived thermal transport in zigzag graphene nanoribbons *Carbon* **113** 292–8

[49] Mortazavi B, Shahrokhi M, Hussain T, Zhuang X and Rabczuk T 2019 Theoretical realization of two-dimensional M3(C6X6)2 (M = Co,Cr,Cu,Fe,Mn,Ni,Pd,Rh and X = O,S, Se) metal–organic frameworks *Appl. Mater. Today* **15** 405–15

[50] Wu C-W, Ren X, Xie G, Zhou W-X, Zhang G and Chen K-Q 2022 Enhanced high-temperature thermoelectric performance by strain engineering in BiOCl *Phys. Rev. Appl.* **18** 014053

[51] Xie Z-X, Liu J-Z, Yu X, Wang H-B, Deng Y-X, Li K-M and Zhang Y 2015 Tunability of acoustic phonon transmission and thermal conductance in three dimensional quasi-periodically stubbed waveguides *J. Appl. Phys.* **117** 114308

[52] Chen X-K, Hu X-Y, Jia P-Z and Xie G-F 2022 First-principles determination of high thermal conductivity of PCF-graphene: a comparison with graphene *Appl. Phys. Lett.* **121** 182205

[53] Chen X-K, Zhang Y, Luo Q-Q, Chen X, Jia P-Z and Zhou W-X 2023 Large contributions from optical phonons to thermal transport in hexagonal carbon-boron-nitrogen monolayers *Phys. Rev.* B **108** 235420

[54] Maintz S, Deringer V L, Tchougréeff A L and Dronskowski R 2016 LOBSTER: a tool to extract chemical bonding from plane-wave based DFT *J. Comput. Chem.* **37** 1030–5

[55] Deringer V L, Tchougréeff A L and Dronskowski R 2011 Crystal orbital Hamilton population (COHP) analysis as projected from plane-wave basis sets *J. Phys. Chem.* A **115** 5461–6